10.1515/msr-2015-0039

MEASUREMENT SCIENCE REVIEW, Volume 15, No. 6, 2015

Image Reconstruction Method with the Exploitation of the Spatial Correlation for Electrical Capacitance Tomography

Jing Lei, Shi Liu

School of Energy, Power and Mechanical Engineering, North China Electric Power University, Changping District,
Beijing 102206, China, leijingdr@126.com (J. Lei), liushidr@yahoo.com (S. Liu)

Electrical capacitance tomography (ECT) is considered to be a competitive measurement method. The imaging objects in ECT measurements are often in a time-varying process, and exploiting the prior information related to the dynamic nature is important for reconstructing high-quality images. Different from existing reconstruction models, in this paper a new model that incorporates the spatial correlation of the pixels by introducing the radial basis function (RBF) method, the dynamic behaviors of a time-varying imaging object, and the ECT measurement information is proposed to formulate the dynamic imaging problem. An objective functional that exploits the spatial correlation of the pixels, the combinational regularizer of the first-order total variation (FOTV) and the second-order total variation (SOTV), the multi-scale regularization, the spatial constraint, and the temporal correlation is proposed to convert the ECT imaging task into an optimization problem. A split Bregman iteration (SBI) method based iteration scheme is developed for solving the proposed objective functional. Numerical simulation results validate the superiority of the proposed reconstruction method on the improvement of the imaging quality.

Keywords: Electrical capacitance tomography, dynamic imaging method, combinational total variation regularization, radial basis function method, spatial correlation property.

1. INTRODUCTION

ECT IS CONSIDERED to be a competitive industrial process tomography method, and has found numerous potential applications in various fields, including the parametric measurements in a multiphase flow system, the visualization measurement of the combustion flame distributions, etc. Over the past decades, the ECT method has been intensively studied, and a large number of advances on theoretical studies and experimental investigations have been achieved.

The reconstruction of high-quality images is useful for the understanding of the underlying physical or chemical mechanisms of the dynamic behaviors of the measurement objects. Various algorithms, including static and dynamic imaging algorithms, were developed for the ECT imaging task. Typical static reconstruction algorithms include the linear back projection method [1], the standard Tikhonov regularization method [2], the Landweber iteration algorithm [3-5], the offline iteration and online reconstruction method [6], the algebraic reconstruction technique [7], the simultaneous iterative reconstruction technique [8], and other static imaging methods found in [9-20]. Representative dynamic reconstruction algorithms include the particle filter method [21], the Kalman filter algorithm [22], the Ensemble Kalman filter method [23], and the four-dimensional imaging algorithm [24]. It should be emphasized that the low imaging quality is a critical bottleneck of restricting practical applications of the ECT measurement method, and the improvement of the imaging quality remains an everlasting concern.

In this paper, we propose a new sequential dynamic reconstruction model that exploits dynamic behaviors and time consistency of a time-varying imaging object and spatial correlation of the pixels. Different from existing static and dynamic imaging models, the RBF method is introduced to investigate the spatial correlation of the pixels. A combinational regularizer of the FOTV and the SOTV is proposed to reconstruct the detailed information of the imaging objects, which is in contrast to available static and dynamic imaging methods. It is noticeable that the introduction of the high-order derivative allows exploiting the spatial correlation of the pixels at different dimensionalities. Additionally, unlike existing ECT imaging methods, a DWT based multi-scale regularizer is introduced to serve as a spatial regularizer. With the utilizations of the spatial correlation of the pixels, the combinational regularizer of the FOTV and the SOTV, the multi-scale regularization, the spatial constraint and the temporal correlation, an objective functional is proposed to convert the ECT imaging task into an optimization problem within the framework of the Tikhonov regularization method. A SBI method based iteration scheme is developed to search for the optimal solution of the proposed objective functional. The effectiveness and advantage of the proposed imaging algorithm are numerically validated.

Along with the main motivations of the work, we organize the rest of this paper as follows. In Section 2, the RBF method is introduced, and a new sequential dynamic model with the consideration of the spatial correlation of the pixels is proposed. In Section 3, the DWT method and the combinational regularizer of the FOTV and the SOTV are introduced, and a new objective functional is proposed to convert the ECT image reconstruction task into an optimization problem. In Section 4, a SBI method based iteration scheme is developed to search for the optimal solution of the proposed objective functional. Section 5 presents numerical results. Finally, we outline the main conclusions in Section 6.

2. SEQUENTIAL DYNAMIC IMAGING MODEL

Seeking an appropriate model to formulate the dynamic imaging problem is useful for practical ECT applications. In this section, common sequential dynamic imaging models and the RBF method are introduced, and a new dynamic imaging model with the exploitations of the spatial correlation of the pixels and the dynamic nature of a time-varying imaging object is proposed.

A. Common sequential dynamic imaging model

There are two categories of mathematical models for the representations of the ECT imaging problem, i.e., static imaging models and dynamic imaging models. Static imaging models had been intensively studied and found numerous applications. However, dynamic imaging models are advantageous on exploiting the dynamic behaviors of a time-varying object. In order to satisfy the practical requirements of dynamic measurements, in this paper we focus on the dynamic imaging model. With a motivation of integrating the dynamic behaviors and the ECT measurement information, the sequential dynamic imaging model can be formulated as:

$$\begin{cases} f(\boldsymbol{G}_\tau, \boldsymbol{v}_\tau) = 0 \\ \boldsymbol{S}_\tau \boldsymbol{G}_\tau + \boldsymbol{U}_\tau = \boldsymbol{C}_\tau + \boldsymbol{r}_\tau \end{cases} \tag{1}$$

where $f(\boldsymbol{G}_\tau, \boldsymbol{v}_\tau) = 0$ describes the dynamic behaviors, and it can be formulated as different equations according to different reconstruction objects; $\boldsymbol{S}_\tau \boldsymbol{G}_\tau + \boldsymbol{U}_\tau = \boldsymbol{C}_\tau + \boldsymbol{r}_\tau$ represents a measurement equation; $\boldsymbol{S}_\tau$ is called the sensitivity matrix in ECT image reconstruction, and it is an $m \times n$ matrix; $\boldsymbol{G}_\tau$ indicates the permittivity distributions, and it is described as an $n \times 1$ vector; $\boldsymbol{C}_\tau$ represents the capacitance values, and it is an $m \times 1$ vector; $\boldsymbol{r}_\tau$ is an $m \times 1$ vector indicating measurement noises; $\boldsymbol{U}_\tau$ represents an $m \times 1$ vector indicating the model deviation; $\boldsymbol{v}_\tau$ depicts the inaccuracy of the dynamic behaviors and subscript τ denotes a discrete time index. For computational simplicity, we approximate $f(\boldsymbol{G}_\tau, \boldsymbol{v}_\tau) = 0$ into $\boldsymbol{G}_\tau = \boldsymbol{F}_\tau \boldsymbol{G}_{\tau-1} + \boldsymbol{v}_\tau$. Consequentially, we can obtain the following sequential dynamic imaging model:

$$\begin{cases} \boldsymbol{G}_\tau = \boldsymbol{F}_\tau \boldsymbol{G}_{\tau-1} + \boldsymbol{v}_\tau \\ \boldsymbol{S}_\tau \boldsymbol{G}_\tau + \boldsymbol{U}_\tau = \boldsymbol{C}_\tau + \boldsymbol{r}_\tau \end{cases} \tag{2}$$

B. Image representation using the RBF method

Exploiting the spatial correlation of the pixels may be useful for the improvement of the imaging quality. Equation (2) utilizes the time-varying behaviors of the imaging objects and the ECT measurement information. However, the exploitation of the correlation of the pixels is omitted. In this section, we employ the RBF method to describe the correlations of the pixels.

According to the RBF method, a pixel value in a two-dimensional image can be approximated as [25], [26]:

$$z(\boldsymbol{x}) = \sum_{j=1}^{M} \boldsymbol{\alpha}_j \varphi(\| \boldsymbol{x} - \boldsymbol{x}_j \|) = \sum_{j=1}^{M} \boldsymbol{\alpha}_j \varphi(\boldsymbol{r}_j) \tag{3}$$

where $\boldsymbol{r}_j = \| \boldsymbol{x} - \boldsymbol{x}_j \|$ and $\varphi(\boldsymbol{r}_j) = \exp(-\boldsymbol{r}_j^2 / 2\sigma^2)$; M is the number of the neighborhood of $\boldsymbol{x}$ and $\varphi(\boldsymbol{r}_j)$ can be predetermined according to a specific reconstruction object.

Obviously, we can compute $z(\boldsymbol{x})$ provided that variable $\boldsymbol{\alpha}_j$ in (3) is solved. According to the RBF method, we can estimate variables $\boldsymbol{\alpha}_j$ via the neighborhood pixel values, which can be formulated as:

$$\begin{bmatrix} \varphi_{1,1} & \cdots & \varphi_{1,M} \\ \vdots & \vdots & \vdots \\ \varphi_{M,1} & \cdots & \varphi_{M,M} \end{bmatrix} \begin{bmatrix} \alpha_1 \\ \vdots \\ \alpha_M \end{bmatrix} = \begin{bmatrix} z_1 \\ \vdots \\ z_M \end{bmatrix} \tag{4}$$

For easy notation, we rewrite (4) as the following system of linear equations:

$$\boldsymbol{AB} = \boldsymbol{Z} \tag{5}$$

where $\boldsymbol{A} = \begin{bmatrix} \varphi_{1,1} & \cdots & \varphi_{1,M} \\ \vdots & \vdots & \vdots \\ \varphi_{M,1} & \cdots & \varphi_{M,M} \end{bmatrix}$, $\boldsymbol{B} = [\alpha_1, \cdots, \alpha_M]^T$ and $\boldsymbol{Z} = [z_1, \cdots, z_M]^T$.

The solution of (5) can be formulated as:

$$\boldsymbol{B} = \boldsymbol{A}^{-1} \boldsymbol{Z} \tag{6}$$

According to (3), finally, the estimation of $z(\boldsymbol{x})$ can be formulated as:

$$z(\boldsymbol{x}) = [\varphi(\| \boldsymbol{x} - \boldsymbol{x}_1 \|), \cdots, \varphi(\| \boldsymbol{x} - \boldsymbol{x}_M \|)] \boldsymbol{A}^{-1} \boldsymbol{Z} \tag{7}$$

For concise expression, (7) can be rewritten as a concise formula:

$$z(\boldsymbol{x}) = \boldsymbol{L}_x \boldsymbol{Z} \tag{8}$$

where $\boldsymbol{L}_x = [\varphi(\| \boldsymbol{x} - \boldsymbol{x}_1 \|), \cdots, \varphi(\| \boldsymbol{x} - \boldsymbol{x}_M \|)] \boldsymbol{A}^{-1}$.

Following the above discussions, we can conclude that one pixel can be locally represented by its neighborhood pixels. The introduction of the spatial correlations is a promising method for ensuring a high-quality imaging result.

C. New sequential dynamic imaging model

Common static and dynamic imaging models fail to exploit the spatial correlation of the pixels. In this section, a new sequential dynamic imaging model is proposed to model the ECT imaging problem, and it can be specified as:

$$\begin{cases} \boldsymbol{G}_\tau = \boldsymbol{F}_\tau \boldsymbol{G}_{\tau-1} + \boldsymbol{v}_\tau \\ \boldsymbol{S}_\tau \boldsymbol{L} \boldsymbol{G}_\tau + \boldsymbol{U}_\tau = \boldsymbol{C}_\tau + \boldsymbol{r}_\tau \end{cases} \tag{9}$$

Equation (9) has two main distinctions. On one hand, the equation incorporates the dynamic behaviors of a time-varying imaging object and the ECT measurement information. On the other hand, the equation exploits the spatial correlation of the pixels.

3. DESIGN OF OBJECTIVE FUNCTIONAL

In this section, we introduce the DWT method and the combinational regularizer of the FOTV and the SOTV, and a new objective functional is proposed to convert (9) into an optimization problem within the framework of the Tikhonov regularization method.

A. Discrete wavelet transform

The wavelet analysis is a particular representation method of signals [27]. Accordingly, a signal $f(t)$ is considered to belong to the scaling space V_0 (i.e., $f(t) \in V_0$), and implementing the multiscale decomposition yields [28], [29]:

$$V_0 = \psi_1 \oplus V_1 = \psi_1 \oplus \psi_2 \oplus \cdots \oplus \psi_\varpi \oplus V_\varpi \tag{10}$$

where ψ_j represents the orthogonal complete place in the jth scale and ϖ stands for a given decomposition scale. We refer the readers to [27-29] for more details.

Essentially, ECT images have two dimensions. In order to remove redundancy between pixels to improve the sparsity of the transform coefficients, a 2D DWT should be employed. Specifically, suppose an ECT image $\boldsymbol{Z}_{n\times n}$ with a dimension of $n \times n$ will be transformed, which can be rearranged as a vector $\boldsymbol{M}_{N\times 1}$, and $N = n \times n$. Finally, the DWT for an image can be formulated as [30-32]:

$$\boldsymbol{\phi} = \boldsymbol{\psi} \boldsymbol{M} \tag{11}$$

where $\boldsymbol{\psi}$ is an equivalent 2D DWT transform matrix.

B. Combinational regularizer of the FOTV and the SOTV

The TV is a popular regularizer [33], and for a 2D image $\boldsymbol{u}$ it can be formulated into the following scheme:

$$\mathrm{TV}(\boldsymbol{u}) = \| \nabla \boldsymbol{u} \|_1 = \| \boldsymbol{D}_x \boldsymbol{u} \|_1 + \| \boldsymbol{D}_y \boldsymbol{u} \|_1 \tag{12}$$

where $\boldsymbol{D}_x$ and $\boldsymbol{D}_y$ are the first-order difference operators.

Equation (12) is a basic formula, which can be extended with different requirements, including the multiple neighborhoods discretization method [34], e.g., the eight weighted neighborhoods discretization, the sixteen weighted neighborhoods discretization, etc., and the combination of the derivatives with different orders [35].

Unlike the multiple neighborhoods discretization methods, the authors in [35] proposed the combinational regularizer of the FOTV and the SOTV, which can be formulated as:

$$\phi(\boldsymbol{u}) = \alpha \mathrm{TV}(\boldsymbol{u}) + \beta \mathrm{TV}^2(\boldsymbol{u}) \tag{13}$$

where α and β are the weighted values. Obviously, (13) is a common TV method when $\alpha = 1$ and $\beta = 0$. For a 2D image, (13) can be specified as:

$$\begin{aligned} \phi(\boldsymbol{u}) = {} & \alpha(\| \boldsymbol{D}_x \boldsymbol{u} \|_1 + \| \boldsymbol{D}_y \boldsymbol{u} \|_1) \\ & + \beta(\| \boldsymbol{D}_{xx} \boldsymbol{u} \|_1 + \| \boldsymbol{D}_{yy} \boldsymbol{u} \|_1 + \| \boldsymbol{D}_{xy} \boldsymbol{u} \|_1 + \| \boldsymbol{D}_{yx} \boldsymbol{u} \|_1) \end{aligned} \tag{14}$$

where $\mathrm{TV}^2(\boldsymbol{u}) = \| \boldsymbol{D}_{xx} \boldsymbol{u} \|_1 + \| \boldsymbol{D}_{yy} \boldsymbol{u} \|_1 + \| \boldsymbol{D}_{xy} \boldsymbol{u} \|_1 + \| \boldsymbol{D}_{yx} \boldsymbol{u} \|_1$; $\boldsymbol{D}_i$ and $\boldsymbol{D}_{ij}$ ($i, j \in \{x, y\}$) stands for difference operators.

C. Objective functional

Finally, we propose a new objective functional to model the ECT imaging problem, which can be formulated as:

$$\min \left\{ \begin{aligned} & \frac{1}{2} \| \boldsymbol{SLG}_\tau + \boldsymbol{U}_\tau - \boldsymbol{C}_\tau \|^2 + \alpha_1 \| \boldsymbol{U}_\tau \|_1 \\ & + \frac{\alpha_2}{2} \| \boldsymbol{G}_\tau - \boldsymbol{G}_{c,\tau} \|^2 + \alpha_3 \sum_{j=1}^{n} (\boldsymbol{W}_{\tau,j} \, | \boldsymbol{G}_{\tau,j} |) \\ & + \frac{\alpha_4}{2} \| \boldsymbol{G}_\tau - \boldsymbol{G}_{\tau-1} \|^2 + \alpha_5 \| \boldsymbol{\psi} \boldsymbol{G}_\tau \|_1 \\ & + \alpha(\| \boldsymbol{D}_x \boldsymbol{u} \|_1 + \| \boldsymbol{D}_y \boldsymbol{u} \|_1) \\ & + \beta(\| \boldsymbol{D}_{xx} \boldsymbol{u} \|_1 + \| \boldsymbol{D}_{yy} \boldsymbol{u} \|_1) \\ & + \beta(\| \boldsymbol{D}_{xy} \boldsymbol{u} \|_1 + \| \boldsymbol{D}_{yx} \boldsymbol{u} \|_1) \end{aligned} \right\} \tag{15}$$

where $\alpha_i > 0$ ($i = 1, 2, \cdots, 5$), $\alpha > 0$ and $\beta > 0$ are called the regularization parameters; $\boldsymbol{G}_{c,\tau}$ represents the dynamic behaviors and can be solved in advance, and $\| \boldsymbol{G}_\tau - \boldsymbol{G}_{c,\tau} \|^2$ integrates the dynamic evolution information into the ECT image reconstruction procedure; $\sum_{j=1}^{n} (\boldsymbol{W}_{\tau,j} \, | \boldsymbol{G}_{\tau,j} |)$ is served as a spatial constraint and $\boldsymbol{W}_{\tau,j}$ stands for a weighted value; $\| \boldsymbol{\psi} \boldsymbol{G}_\tau \|_1$ represents a multi-scale regularizer; $\| \boldsymbol{SLG}_\tau + \boldsymbol{U}_\tau - \boldsymbol{C}_\tau \|^2$ measures the data fidelity and considers the spatial correlations of the pixels, and $\boldsymbol{L}$ can be obtained via solving (8).

Equation (15) is consistent with the framework of the Tikhonov regularization method, and we can outline the appealing properties as follows.

1) The dynamic behaviors of a time-varying imaging object and the ECT measurement information are incorporated into the proposed objective functional. Moreover, the inaccurate properties of the reconstruction model and the measurement data are simultaneously highlighted, which is consistent with real-world applications since the inaccuracies of the input data are ubiquitous.

2) Unlike existing ECT imaging methods, including static and dynamic imaging algorithms, the spatial dependence of the pixels is exploited by the RBF method.

3) The combinational regularizer of the FOTV and the SOTV is introduced to the objective functional to serve as the spatial regularizer. The introduction of the high-order derivative will be beneficial for the exploitation of the spatial correlation of the pixels.

4) In contrast to available ECT imaging methods, a 2D DWT based multi-scale regularizer is incorporated into the objective functional.

5) The Tikhonov regularization method is employed to impose the prior constraints associated with the dynamic properties of a time-varying object and weaken the numerical instability derived from the ill-posedness of the ECT imaging problem.

4. SOLVING THE OBJECTIVE FUNCTIONAL

In previous sections, we converted the ECT image reconstruction procedure into an optimization problem within the framework of the Tikhonov regularization method with the additive constraints related to the underlying imaging objects. In this section, a SBI method based iteration scheme is developed to solve (15).

According to the computational strategy presented in [36-42], (15) can be decoupled as:

$$\boldsymbol{U}_\tau^{k+1} = \min\left\{\frac{1}{2}\|\boldsymbol{SLG}_\tau^k + \boldsymbol{U}_\tau - \boldsymbol{C}_\tau\|^2 + \alpha_1\|\boldsymbol{U}_\tau\|_1\right\} \tag{16}$$

$$\boldsymbol{G}_\tau^{k+1} = \min\left\{\begin{array}{l} \frac{1}{2}\|\boldsymbol{SLG}_\tau + \boldsymbol{U}_\tau^{k+1} - \boldsymbol{C}_\tau\|^2 + \frac{\alpha_2}{2}\|\boldsymbol{G}_\tau - \boldsymbol{G}_{c,\tau}\|^2 \\ +\alpha_3\sum_{j=1}^{n}(\boldsymbol{W}_{\tau,j}\,|\boldsymbol{G}_{\tau,j}|) + \frac{\alpha_4}{2}\|\boldsymbol{G}_\tau - \boldsymbol{G}_{\tau-1}\|^2 \\ +\alpha_5\|\boldsymbol{\psi G}_\tau\|_1 + \alpha(\|\boldsymbol{D}_x\boldsymbol{G}_\tau\|_1 + \|\boldsymbol{D}_y\boldsymbol{G}_\tau\|_1) \\ +\beta(\|\boldsymbol{D}_{xx}\boldsymbol{G}_\tau\|_1 + \|\boldsymbol{D}_{yy}\boldsymbol{G}_\tau\|_1 + \|\boldsymbol{D}_{xy}\boldsymbol{G}_\tau\|_1 + \|\boldsymbol{D}_{yx}\boldsymbol{G}_\tau\|_1) \end{array}\right\} \tag{17}$$

Theoretically, the direct computation of (17) is an intractable task. In order to make the problem tractable, we rewrite (17) into a constrained optimization problem by introducing corresponding equality constraints:

$$\left\{\begin{array}{l} \min\left\{\begin{array}{l} \frac{1}{2}\|\boldsymbol{SLG}_\tau + \boldsymbol{U}_\tau^{k+1} - \boldsymbol{C}_\tau\|^2 + \frac{\alpha_2}{2}\|\boldsymbol{G}_\tau - \boldsymbol{G}_{c,\tau}\|^2 \\ +\alpha_3\sum_{j=1}^{n}(\boldsymbol{W}_{\tau,j}\,|\boldsymbol{G}_{\tau,j}|) + \frac{\alpha_4}{2}\|\boldsymbol{G}_\tau - \boldsymbol{G}_{\tau-1}\|^2 \\ +\alpha_5\|\boldsymbol{d}_{7,\tau}\|_1 + \alpha(\|\boldsymbol{d}_{1,\tau}\|_1 + \|\boldsymbol{d}_{2,\tau}\|_1) \\ +\beta(\|\boldsymbol{d}_{3,\tau}\|_1 + \|\boldsymbol{d}_{4,\tau}\|_1 + \|\boldsymbol{d}_{5,\tau}\|_1 + \|\boldsymbol{d}_{6,\tau}\|_1) \end{array}\right\} \\ s.t.\ \boldsymbol{d}_{1,\tau} = \boldsymbol{D}_x\boldsymbol{G}_\tau, \boldsymbol{d}_{2,\tau} = \boldsymbol{D}_y\boldsymbol{G}_\tau, \boldsymbol{d}_{3,\tau} = \boldsymbol{D}_{xx}\boldsymbol{G}_\tau \\ \boldsymbol{d}_{4,\tau} = \boldsymbol{D}_{yy}\boldsymbol{G}_\tau, \boldsymbol{d}_{5,\tau} = \boldsymbol{D}_{xy}\boldsymbol{G}_\tau, \boldsymbol{d}_{6,\tau} = \boldsymbol{D}_{yx}\boldsymbol{G}_\tau, \boldsymbol{d}_{7,\tau} = \boldsymbol{\psi G}_\tau \end{array}\right. \tag{18}$$

Within the framework of the SBI method [43], we rewrite (18) as:

$$\min\left\{\begin{array}{l} \frac{1}{2}\|\boldsymbol{SLG}_\tau + \boldsymbol{U}_\tau^{k+1} - \boldsymbol{C}_\tau\|^2 + \frac{\alpha_2}{2}\|\boldsymbol{G}_\tau - \boldsymbol{G}_{c,\tau}\|^2 \\ +\alpha_3\sum_{j=1}^{n}(\boldsymbol{W}_{\tau,j}\,|\boldsymbol{G}_{\tau,j}|) + \frac{\alpha_4}{2}\|\boldsymbol{G}_\tau - \boldsymbol{G}_{\tau-1}\|^2 \\ +\alpha(\|\boldsymbol{d}_{1,\tau}\|_1 + \|\boldsymbol{d}_{2,\tau}\|_1) \\ +\beta(\|\boldsymbol{d}_{3,\tau}\|_1 + \|\boldsymbol{d}_{4,\tau}\|_1 + \|\boldsymbol{d}_{5,\tau}\|_1 + \|\boldsymbol{d}_{6,\tau}\|_1) \\ +\alpha_5\|\boldsymbol{d}_{7,\tau}\|_1 + \frac{\mu_1}{2}\|\boldsymbol{d}_{1,\tau} - \boldsymbol{D}_x\boldsymbol{G}_\tau - \boldsymbol{b}_{1,\tau}^k\|^2 \\ +\frac{\mu_2}{2}\|\boldsymbol{d}_{2,\tau} - \boldsymbol{D}_y\boldsymbol{G}_\tau - \boldsymbol{b}_{2,\tau}^k\|^2 + \frac{\mu_3}{2}\|\boldsymbol{d}_{3,\tau} - \boldsymbol{D}_{xx}\boldsymbol{G}_\tau - \boldsymbol{b}_{3,\tau}^k\|^2 \\ +\frac{\mu_4}{2}\|\boldsymbol{d}_{4,\tau} - \boldsymbol{D}_{yy}\boldsymbol{G}_\tau - \boldsymbol{b}_{4,\tau}^k\|^2 + \frac{\mu_5}{2}\|\boldsymbol{d}_{5,\tau} - \boldsymbol{D}_{xy}\boldsymbol{G}_\tau - \boldsymbol{b}_{5,\tau}^k\|^2 \\ +\frac{\mu_6}{2}\|\boldsymbol{d}_{6,\tau} - \boldsymbol{D}_{yx}\boldsymbol{G}_\tau - \boldsymbol{b}_{6,\tau}^k\|_1 + \frac{\mu_7}{2}\|\boldsymbol{d}_{7,\tau} - \boldsymbol{\psi G}_\tau - \boldsymbol{b}_{7,\tau}^k\|^2 \end{array}\right\} \tag{19}$$

$$\boldsymbol{b}_{1,\tau}^{k+1} = \boldsymbol{b}_{1,\tau}^{k} - (\boldsymbol{d}_{1,\tau}^{k+1} - \boldsymbol{D}_x\boldsymbol{G}_\tau^{k+1}) \tag{20}$$

$$\boldsymbol{b}_{2,\tau}^{k+1} = \boldsymbol{b}_{2,\tau}^{k} - (\boldsymbol{d}_{2,\tau}^{k+1} - \boldsymbol{D}_y\boldsymbol{G}_\tau^{k+1}) \tag{21}$$

$$\boldsymbol{b}_{3,\tau}^{k+1} = \boldsymbol{b}_{3,\tau}^{k} - (\boldsymbol{d}_{3,\tau}^{k+1} - \boldsymbol{D}_{xx}\boldsymbol{G}_\tau^{k+1}) \tag{22}$$

$$\boldsymbol{b}_{4,\tau}^{k+1} = \boldsymbol{b}_{4,\tau}^{k} - (\boldsymbol{d}_{4,\tau}^{k+1} - \boldsymbol{D}_{yy}\boldsymbol{G}_\tau^{k+1}) \tag{23}$$

$$\boldsymbol{b}_{5,\tau}^{k+1} = \boldsymbol{b}_{5,\tau}^{k} - (\boldsymbol{d}_{5,\tau}^{k+1} - \boldsymbol{D}_{xy}\boldsymbol{G}_\tau^{k+1}) \tag{24}$$

$$\boldsymbol{b}_{6,\tau}^{k+1} = \boldsymbol{b}_{6,\tau}^{k} - (\boldsymbol{d}_{6,\tau}^{k+1} - \boldsymbol{D}_{yx}\boldsymbol{G}_\tau^{k+1}) \tag{25}$$

$$\boldsymbol{b}_{7,\tau}^{k+1} = \boldsymbol{b}_{7,\tau}^{k} - (\boldsymbol{d}_{7,\tau}^{k+1} - \boldsymbol{\psi G}_\tau^{k+1}) \tag{26}$$

Similarly, (19) can be decoupled as:

$$\boldsymbol{d}_{1,\tau}^{k+1} = \min\left\{\alpha\|\boldsymbol{d}_{1,\tau}\|_1 + \frac{\mu_1}{2}\|\boldsymbol{d}_{1,\tau} - \boldsymbol{D}_x\boldsymbol{G}_\tau - \boldsymbol{b}_{1,\tau}^k\|^2\right\} \tag{27}$$

$$\boldsymbol{d}_{2,\tau}^{k+1}=\min\left\{\alpha\,\|\boldsymbol{d}_{2,\tau}\|_1+\frac{\mu_2}{2}\|\boldsymbol{d}_{2,\tau}-\boldsymbol{D}_y\boldsymbol{G}_\tau-\boldsymbol{b}_{2,\tau}^k\|^2\right\} \tag{28}$$

$$\boldsymbol{d}_{3,\tau}^{k+1}=\min\left\{\beta\,\|\boldsymbol{d}_{3,\tau}\|_1+\frac{\mu_3}{2}\|\boldsymbol{d}_{3,\tau}-\boldsymbol{D}_{xx}\boldsymbol{G}_\tau-\boldsymbol{b}_{3,\tau}^k\|^2\right\} \tag{29}$$

$$\boldsymbol{d}_{4,\tau}^{k+1}=\min\left\{\beta\,\|\boldsymbol{d}_{4,\tau}\|_1+\frac{\mu_4}{2}\|\boldsymbol{d}_{4,\tau}-\boldsymbol{D}_{yy}\boldsymbol{G}_\tau-\boldsymbol{b}_{4,\tau}^k\|^2\right\} \tag{30}$$

$$\boldsymbol{d}_{5,\tau}^{k+1}=\min\left\{\beta\,\|\boldsymbol{d}_{5,\tau}\|_1+\frac{\mu_5}{2}\|\boldsymbol{d}_{5,\tau}-\boldsymbol{D}_{xy}\boldsymbol{G}_\tau-\boldsymbol{b}_{5,\tau}^k\|^2\right\} \tag{31}$$

$$\boldsymbol{d}_{6,\tau}^{k+1}=\min\left\{\beta\,\|\boldsymbol{d}_{6,\tau}\|_1+\frac{\mu_6}{2}\|\boldsymbol{d}_{6,\tau}-\boldsymbol{D}_{yx}\boldsymbol{G}_\tau-\boldsymbol{b}_{6,\tau}^k\|^2\right\} \tag{32}$$

$$\boldsymbol{d}_{7,\tau}^{k+1}=\min\left\{\alpha_5\,\|\boldsymbol{d}_{7,\tau}\|_1+\frac{\mu_7}{2}\|\boldsymbol{d}_{7,\tau}-\boldsymbol{\psi}\boldsymbol{G}_\tau-\boldsymbol{b}_{7,\tau}^k\|^2\right\} \tag{33}$$

$$\boldsymbol{G}_\tau^{k+1}=\min\left\{\begin{aligned}&\frac{1}{2}\|\boldsymbol{SLG}_\tau+\boldsymbol{U}_\tau^{k+1}-\boldsymbol{C}_\tau\|^2+\frac{\alpha_2}{2}\|\boldsymbol{G}_\tau-\boldsymbol{G}_{c,\tau}\|^2+\alpha_3\sum_{j=1}^{n}(\boldsymbol{W}_{\tau,j}\,|\boldsymbol{G}_{\tau,j}|)\\&+\frac{\alpha_4}{2}\|\boldsymbol{G}_\tau-\boldsymbol{G}_{\tau-1}\|^2+\frac{\mu_1}{2}\|\boldsymbol{d}_{1,\tau}^{k+1}-\boldsymbol{D}_x\boldsymbol{G}_\tau-\boldsymbol{b}_{1,\tau}^k\|^2\\&+\frac{\mu_2}{2}\|\boldsymbol{d}_{2,\tau}^{k+1}-\boldsymbol{D}_y\boldsymbol{G}_\tau-\boldsymbol{b}_{2,\tau}^k\|^2+\frac{\mu_3}{2}\|\boldsymbol{d}_{3,\tau}^{k+1}-\boldsymbol{D}_{xx}\boldsymbol{G}_\tau-\boldsymbol{b}_{3,\tau}^k\|^2\\&+\frac{\mu_4}{2}\|\boldsymbol{d}_{4,\tau}^{k+1}-\boldsymbol{D}_{yy}\boldsymbol{G}_\tau-\boldsymbol{b}_{4,\tau}^k\|^2+\frac{\mu_5}{2}\|\boldsymbol{d}_{5,\tau}^{k+1}-\boldsymbol{D}_{xy}\boldsymbol{G}_\tau-\boldsymbol{b}_{5,\tau}^k\|^2\\&+\frac{\mu_6}{2}\|\boldsymbol{d}_{6,\tau}^{k+1}-\boldsymbol{D}_{yx}\boldsymbol{G}_\tau-\boldsymbol{b}_{6,\tau}^k\|_1+\frac{\mu_7}{2}\|\boldsymbol{d}_{7,\tau}^{k+1}-\boldsymbol{\psi}\boldsymbol{G}_\tau-\boldsymbol{b}_{7,\tau}^k\|^2\end{aligned}\right\} \tag{34}$$

According to the above discussions, finally, we developed an iteration scheme to solve (15), and the numerical procedure can be summarized as follows:

Step 1. Specify the algorithmic parameters and the initial value, and set $\tau=1$.

Step 2. Update variable $\boldsymbol{U}_\tau^{k+1}$ by solving (16).

Step 3. Update variables $\boldsymbol{d}_{j,\tau}^{k+1}$ via solving (27-33).

Step 4. Update variable $\boldsymbol{G}_\tau^{k+1}$ by solving (34).

Step 5. Update variables $\boldsymbol{b}_{j,\tau}^{k+1}$ according to (20-26).

Step 6. Loop to Step 2 until a predetermined iteration stopping criterion is satisfied.

Step 7. Set $\tau\leftarrow\tau+1$, loop to Step 2 until the maximum time index is met.

Commonly, we know in advance that the inversion solution belongs to the range $[q_1,q_2]$, therefore, a projected operator is introduced to the iteration scheme:

$$\boldsymbol{G}_\tau^{k+1}=\text{Project}\left\{\boldsymbol{G}_\tau^{k+1}\right\} \tag{35}$$

where

$$\text{Project}[\boldsymbol{Q}_j]=\begin{cases}q_1, & \boldsymbol{Q}_j<q_1\\ \boldsymbol{Q}_j, & q_1\le\boldsymbol{Q}_j\le q_2\\ q_2, & \boldsymbol{Q}_j>q_2\end{cases} \tag{36}$$

5. NUMERICAL SIMULATIONS AND DISCUSSIONS

In the proposed imaging method, we use the iteration scheme presented in Section 4 to solve (15), and it can be called the radial basis function based dynamic reconstruction (RBFDR) algorithm. In this section, we numerically evaluate the feasibility and the robustness of the RBFDR algorithm, and the imaging results are compared with the OIOR method and the projected Landweber iteration (PLI) algorithm.

We employ a 12-electrode square ECT sensor for simulations, and the images are visualized using 32×32 pixels. The size of the reconstruction domain is 80×80 mm^2, and the diameter of the bubbles is 20 mm. The capacitance data are computed using the finite element method based on the Ansoft software platform.

Owing to the limitation of the numerical simulation, we use the purely random-walk evolution model, i.e., $\boldsymbol{F}_\tau=\boldsymbol{I}$ and $\boldsymbol{I}$ is an identity matrix. The model is often used in practices when a better temporal dynamic model is not known [22].

All reconstruction methods are implemented on the MATLAB 7.0 software platform. The stopping criterion of iterations for the RBFDR algorithm is defined as $\|\boldsymbol{G}^{k+1}-\boldsymbol{G}^k\|/\|\boldsymbol{G}^{k+1}\|<1\times10^{-3}$. The image error is used to evaluate the quality of an inversion solution, and it is specified as:

$$\gamma=\frac{\|\boldsymbol{G}_{\text{Original}}-\boldsymbol{G}_{\text{Reconstructed}}\|}{\|\boldsymbol{G}_{\text{Original}}\|}\times100\% \tag{37}$$

where γ is the imager error; $\boldsymbol{G}_{\text{Original}}$ and $\boldsymbol{G}_{\text{Reconstructed}}$ stand for the original and reconstructed values, respectively.

A. Case 1

A dynamic reconstruction case is implemented to evaluate the RBFDR algorithm. We illustrate the original dynamic imaging objects at different discrete time instants in Fig.1. Table 1. lists the algorithmic parameters for the PLI method, and the number of iterations corresponds to the minimum image errors for fair comparison. As for the RBFDR algorithm, the algorithmic parameters are empirically set as $\alpha=1$, $\beta=1$, $\alpha_1=0.1$, $\alpha_2=10^{-5}$, $\alpha_3=0.005$, $\alpha_4=10^{-5}$, $\alpha_5=1$, $\boldsymbol{W}_{\tau,j}=1/(|\boldsymbol{G}_{\tau-1,j}|^p+\varepsilon)$, $p=2$ and $\varepsilon=10^{-10}$. The Daubechies 4 wavelet is used to implement the multi-scale analysis. We compute the initial values via the STR method. The imaging results of the OIOR algorithm, the PLI method and the RBFDR algorithm are presented in Fig.2. - Fig.4., respectively. We list the image errors and the computational time in Table 2. and Table 3., respectively.

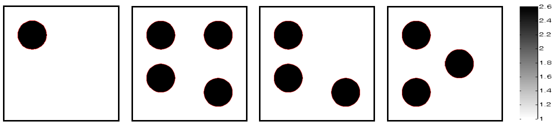

1.a) 1.b) 1.c) 1.d)

Fig.1. Dynamic reconstruction objects.

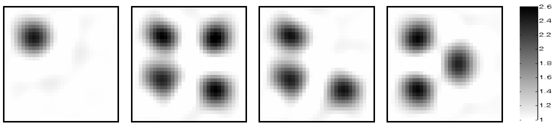

2.a) 2.b) 2.c) (2.d)

Fig.2. Reconstructed images by the OIOR algorithm.

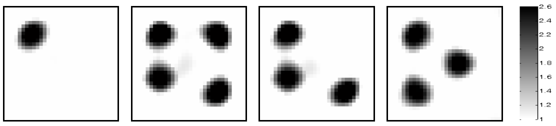

3.a) 3.b) 3.c) 3.d)

Fig.3. Reconstructed images by the PLI algorithm.

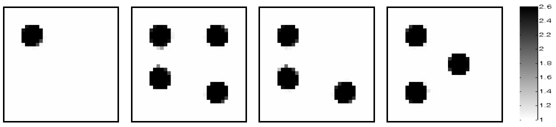

4.a) 4.b) 4.c) 4.d)

Fig.4. Reconstructed images by the RBFDR algorithm.

Table 1. Algorithmic parameters for the PLI algorithm.

Algorithmic parameters	**Fig.1(a)**	**Fig.1(b)**	**Fig.1(c)**	**Fig.1(d)**
Relaxation factor	1	1	1	1
Number of iteration	324	432	448	401

Table 2. Image errors (%).

Algorithms	**Fig.1(a)**	**Fig.1(b)**	**Fig.1(c)**	**Fig.1(d)**
OIOR	15.76	25.32	23.63	23.47
PLI	11.59	18.82	17.50	15.09
RBFDR	1.95	3.60	3.88	1.87

Table 3. Computational time (s).

Algorithms	**Fig.1(a)**	**Fig.1(b)**	**Fig.1(c)**	**Fig.1(d)**
PLI	0.46	0.61	0.63	0.57
RBFDR	8.90	11.14	11.79	12.75

The OIOR method benefits from the online reconstruction property. However, applying the OIOR method to deal with the time-varying objects will suffer from the following practical problems: 1) the smoothness effect of the OIOR method blurs the detailed information of the reconstructed images, 2) the OIOR method omits the prior information related to dynamic properties of the time-varying imaging objects, and 3) the images are independently reconstructed one by one, and the considerations of the inter-frame correlation of the images are absent. The above disadvantages restrict the improvement of the imaging quality. In fact, we can observe from Fig.2. that the OIOR method leads to noticeable reconstruction artifacts. Meanwhile, according to the results listed in Table 2., we can find that the image errors of the OIOR method for original imaging objects shown in Fig.1.a) – Fig.1.d) are 15.76 %, 25.32 %, 23.63 % and 23.47 %, which are far higher than the PLI method and the RBFDR algorithm.

Studies indicate that the PLI method benefits from the following two aspects: (1) the numerical procedure of the PLI method is easy and the computational complexity and cost are low, and (2) the final inversion solution is insensitive to the selection of the initial solutions. These superiorities lead to the wide applications of the PLI method. Unfortunately, the PLI algorithm does not utilize the prior knowledge related to the dynamic behaviors of the time-varying imaging objects. Furthermore, the absence of the utilization of the spatial correlations of the pixels also results in the limitation of the improvement of the imaging quality. In fact, the results presented in Fig.3. and Table 2. indicate that the PLI method leads to significant artifacts, and the image errors for the original imaging objects are 11.59 %, 18.82 %, 17.50 % and 15.09 %.

Numerical simulation results indicate that the numerical stability of the RBFDR algorithm is associated with the fact that the Tikhonov regularization technique is introduced to the proposed objective functional. Different from existing imaging methods, especially the RBFDR method takes into consideration the spatial correlation of the pixels, the combinational regularizer of the FOTV and the SOTV, the multi-scale regularization, the spatial constraint, and the temporal correlation of a time-varying imaging object, which leads to the increase of the imaging quality. The results shown in Fig.4. confirm the fact.

The acquisition of high-quality images is desired for the understanding of the underlying physical or chemical mechanisms of the dynamic behaviors of the imaging objects. In Table 2., the image errors of the RBFDR algorithm for imaging objects presented in Fig.1.a) - Fig.1.d), are 1.95 %, 3.60 %, 3.88 % and 1.87 %, which is far smaller than the OIOR method and the PLI algorithm.

The OIOR algorithm benefits from the online reconstruction property, which is a useful feature for practical applications. We list the computational time for the PLI method and the RBFDR algorithm in Table 3. It can be observed that for the original imaging objects presented in Fig.1.a) - Fig.1.d) the computational time of the RBFDR method is more than the PLI method. In the future, more investigations on the improvement of the reconstruction speed should be further conducted.

B. Case 2

The ill-posedness of the ECT imaging problem makes the final inversion solution sensitive to the inaccurate properties of the input data. In this section, we use the noise-contaminated capacitance data to evaluate the robustness of the RBFDR algorithm, and the noise level is defined as:

$$\eta = \frac{\| \boldsymbol{C}_{\text{Original}} - \boldsymbol{C}_{\text{Contaminated}} \|}{\| \boldsymbol{C}_{\text{Original}} \|} \times 100\% \tag{38}$$

where η is the noise level; $\boldsymbol{C}_{\text{Original}}$ and $\boldsymbol{C}_{\text{Contaminated}}$ are the original and contaminated capacitance data, respectively; $\boldsymbol{C}_{\text{Contaminated}} = \boldsymbol{C}_{\text{Original}} + \sigma\delta$, σ represents the standard deviation and δ stands for a normal distribution random number with mean 0 and standard deviation 1.

The algorithmic parameters for the RBFDR algorithm are the same as in Section 5.A. We show the imaging results of the RBFDR algorithm under the noise levels of 6 % and 15 % in Fig.5. and Fig.6., respectively. The image errors under different noise levels are illustrated in Table 4.

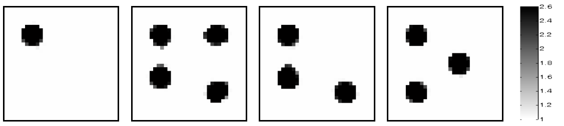

5.a) 5.b) 5.c) 5.d)

Fig.5. Reconstructed images by the RBFDR algorithm under the noise level of 6 %.

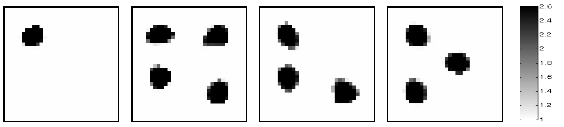

6.a) 6.b) 6.c) 6.d)

Fig.6. Reconstructed images by the RBFDR algorithm under the noise level of 15 %.

Table 4. Image errors under different noise levels (%).

Noise levels	Fig.1(a)	Fig.1(b)	Fig.1(c)	Fig.1(d)
6%	2.30	9.90	5.61	3.67
15%	8.07	15.16	13.04	11.42

Fig.5. and Fig.6. are the imaging results of the RBFDR algorithm when the noise levels of the capacitance data are 6 % and 15 %, respectively. According to the results presented in Fig.5. and Fig.6., we find that the RBFDR algorithm shows a good robustness, and the imaging quality of the RBFDR algorithm under different noise levels is satisfactory. In Table 4., when the noise level is 15 %, the image errors are 8.07 %, 15.16 %, 13.04 % and 11.42 %, which validates that the RBFDR algorithm is able to deal with the inaccuracy of the measurement data. It should be pointed out that such advantages benefit from the fact that within the framework of the Tikhonov regularization method, the inaccurate properties of the reconstruction model and the measurement data are simultaneously emphasized in the RBFDR algorithm.

C. Case 3

In real-world applications, the imaging model may be inaccurately derived from physically implementing an imperfect ECT sensor and the linearization approximation of the reconstruction model. In this section, the influence of the inaccuracies of the reconstruction model and the measurement data on the imaging quality is numerically evaluated. In this paper, the sensitivity matrix is perturbed to simulate the inaccuracy of the reconstruction model. The inaccuracy of the sensitivity matrix is defined as:

$$\boldsymbol{S}_{\text{contaminated}} = \boldsymbol{S}_{\text{original}} + \boldsymbol{E} \tag{39}$$

where $\boldsymbol{E} = \sigma \cdot randn$, and σ is the standard deviation; $\boldsymbol{S}_{\text{original}}$ and $\boldsymbol{S}_{\text{contaminated}}$ stand for original and noise-contaminated sensitivity matrices, respectively.

Fig.7. and Fig.8. illustrate the imaging results of the RBFDR algorithm when the inaccurate properties of the sensitivity matrix and the measurement data are simultaneously considered, and the image errors are presented in Table 5.

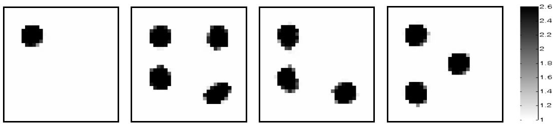

7.a) 7.b) 7.c) 7.d)

Fig.7. Reconstructed images when the standard deviation of the sensitivity matrix and the noise level of the capacitance data are 0.001 and 5 %.

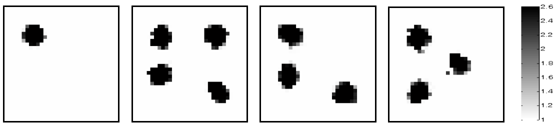

8.a) 8.b) 8.c) 8.d)

Fig.8. Reconstructed images when the standard deviation of the sensitivity matrix and the noise level of the capacitance data are 0.003 and 9 %.

Table 5. Image errors (%).

Noise levels	Standard deviations	Fig.1(a)	Fig.1(b)	Fig.1(c)	Fig.1(d)
5%	$\sigma = 0.001$	3.02	13.79	10.72	4.83
9%	$\sigma = 0.003$	8.89	22.30	17.16	17.88

In Fig.7. and Fig.8., we report the imaging results of the RBFDR algorithm when the inaccurate properties of the sensitivity matrix and the measurement data are simultaneously considered. We can observe from Fig.7. and

Fig.8. that the introduction of the inaccurate properties on the measurement data and the imaging model into the proposed objective functional is able to improve the robustness of the RBFDR algorithm. In Table 5., when the standard deviation of the sensitivity matrix is 0.003 and the noise level of the capacitance data is 9 %, the image errors for the original dynamic imaging objects in Fig.1.a) - Fig.1.d) are 8.89 %, 22.30 %, 17.16 % and 17.88 %, which confirms that the RBFDR algorithm is robust to the inaccuracies of the imaging model and the measurement data. This property is highly beneficial for real-world applications.

D. Case 4

In this section we use the imaging objects with the high contrast permittivity distributions to further evaluate the feasibility of the RBFDR method. Fig.9. shows the imaging objects, in which the black part represents the high permittivity, i.e., 81, and the white part stands for the low permittivity, i.e., 1.0. The algorithmic parameters for the RBFDR algorithm are empirically set as $\alpha = 1$, $\beta = 1$, $\alpha_1 = 0.5$, $\alpha_2 = 10^{-4}$, $\alpha_3 = 0.0035$, $\alpha_4 = 10^{-4}$, $\alpha_5 = 1$, $\boldsymbol{W}_{\tau,j} = 1/(|\boldsymbol{G}_{\tau-1,j}|^p + \varepsilon)$ and $p = 3.5$. The algorithmic parameters of the PLI method are listed in Table 6. Fig.10. - Fig.12. demonstrate the image reconstruction by the OIOR method, the PLI algorithm and the RBFDR method, respectively. The image errors for the compared reconstruction methods are shown in Table 7.

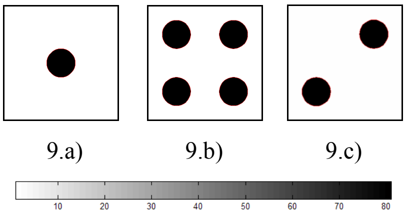
9.a) 9.b) 9.c)

Fig.9. Dynamic reconstruction objects.

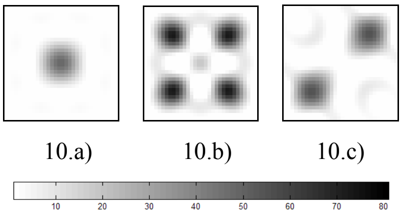
10.a) 10.b) 10.c)

Fig.10. Reconstructed images by the OIOR algorithm.

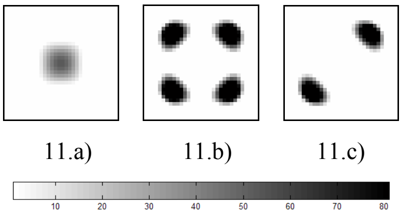
11.a) 11.b) 11.c)

Fig.11. Reconstructed images by the PLI algorithm.

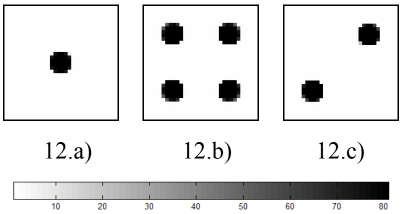
12.a) 12.b) 12.c)

Fig.12. Reconstructed images by the RBFDR algorithm.

Table 6. Algorithmic parameters for the PLI algorithm.

Algorithmic parameters	**Fig.9(a)**	**Fig.9(b)**	**Fig.9(c)**
Relaxation factor	1	1	1
Number of iteration	235	81	146

Table 7. Image errors (%).

Algorithms	**Fig.9(a)**	**Fig.9(b)**	**Fig.9(c)**
OIOR	64.53	52.19	63.73
PLI	60.80	39.39	39.80
RBFDR	4.40	9.68	7.28

Fig.10. - Fig.12. show the imaging results reconstructed by the OIOR method, the PLI algorithm and the RBFDR method when the difference of the permittivity in the reconstruction domain is large. We can observe that the reconstruction quality of the RBFDR method is higher than the OIOR method and the PLI algorithm. In fact, we can find from Table 7. that the image errors of the RBFDR method for the original dynamic imaging objects shown in Fig.9.a) - Fig.9.c) are 4.40 %, 9.68 % and 7.28 %, which are lower than the OIOR method and the PLI algorithm. These imaging results confirm that the RBFDR method may be a promising candidate for the ECT image reconstruction problem.

Following the simulation results from the noise-free and noise-contaminated capacitance data, presented in previous sections, we can conclude that the RBFDR algorithm is successful in dealing with the dynamic imaging tasks. More importantly, we present a new framework for solving the ECT inverse problem, which may be extended to image reconstruction problems in other related fields, such as the electrical resistance tomography, the electrical impedance tomography, etc.

6. CONCLUSIONS

The reconstruction of the high-quality images plays a crucial role in real-world applications of the ECT method. Different from existing imaging models, in this paper a dynamic imaging model that incorporates the spatial correlation of the pixels, the dynamic behaviors of a time-varying imaging object and the ECT measurement information is proposed to formulate the dynamic imaging problem. An objective functional that exploits the spatial correlation of the pixels, the combinational regularizer of the FOTV and the SOTV, the multi-scale regularization, the spatial constraint and the temporal correlation is proposed to convert the ECT imaging task into an optimization problem within the framework of the Tikhonov regularization method. An iteration scheme that integrates the advantages of the SBI method is developed to search for the optimal solution of the proposed objective functional. Numerical results validate the advantage of the proposed reconstruction method on the improvement of the imaging quality. Furthermore, this paper presents a new perspective to deal with the ECT imaging problem, and it can be extended to solve the inverse problems in other tomography technologies.

Practical applications and theoretical studies indicate that one reconstruction method may illustrate different numerical performances to different imaging objects, and the selection of a specific reconstruction method depends mainly on the measurement requirements, the understandings of the prior knowledge related to the imaging objects and the properties of the numerical method. Our work provides an alternative approach for solving the ECT inverse problem, which needs to be further validated by more cases in the future and to be further studied on the respects, including the reconstruction model, the computational strategy, etc.

ACKNOWLEDGEMENTS

The authors thank the National Natural Science Foundation of China (No. 51206048) and the Fundamental Research Funds for the Central Universities (No. 13MS11) for supporting this research.

REFERENCES

[1] Xie, C.G., Huang, S.M., Hoyle, B.S., Thorn, R., Lenn, C., Snowden, D., Beck, M.S. (1992). Electrical capacitance for flow imaging: system model for development of image reconstruction algorithms and design of primary sensors. *IEE Proceedings G - Circuits, Devices and Systems*, 139 (1), 89–98.

[2] Tikhonov, A.N., Arsenin, V.Y. (1977). *Solution of Ill-Posed Problems*. New York: V.H. Winston & Sons.

[3] Landweber, L. (1951). An iteration formula for fredholm integral equations of the first kind. *American Journal of Mathematics*, 73 (3), 615–624.

[4] Yang, W.Q., Spink, D.M., York, T.A., McCann, H. (1999). An image reconstruction algorithm based on Landweber's iteration method for electrical capacitance tomography. *Measurement Science and Technology*, 10 (11), 1065–1069.

[5] Jang, J.D., Lee, S.H., Kim, K.Y., Choi, B.Y. (2006). Modified iterative Landweber method in electrical capacitance tomography. *Measurement Science and Technology*, 17 (7), 1909–1917.

[6] Liu, S., Fu, L., Yang, W.Q., Wang, H.G., Jiang, F. (2004). Prior-online iteration for image reconstruction with electrical capacitance tomography. *IEE Proceedings - Science, Measurement and Technology*, 151 (3), 195–200.

[7] Yang, W.Q., Peng, L.H. (2003). Image reconstruction algorithms for electrical capacitance tomography. *Measurement Science and Technology*, 14 (1), L1–L13.

[8] Su, B.L., Zhang, Y.H., Peng, L.H., Yao, D.Y., Zhang, B.F. (2000). The use of simultaneous iterative reconstruction technique for electrical capacitance tomography. *Chemical Engineering Journal*, 77 (1), 37–41.

[9] Mou, C.H., Peng, L.H., Yao, D.Y., Xiao, D.Y. (2005). Image reconstruction using a genetic algorithm for electrical capacitance tomography. *Tsinghua Science and Technology*, 10 (5), 587–592.

[10] Takei, M. (2006). GVSPM image reconstruction for capacitance CT images of particles in a vertical pipe and comparison with the conventional method. *Measurement Science and Technology*, 17 (8), 2104–2112.

[11] Soleimani, M., Lionheart, W.R.B. (2005). Nonlinear image reconstruction for electrical capacitance tomography using experimental data. *Measurement Science and Technology*, 16 (10), 1987–1996.

[12] Wang, H.X., Tang, L., Cao, Z. (2007). An image reconstruction algorithm based on total variation with adaptive mesh refinement for ECT. *Flow Measurement and Instrumentation*, 18 (5–6), 262–267.

[13] Fang, W.F. (2004). A nonlinear image reconstruction algorithm for electrical capacitance tomography. *Measurement Science and Technology*, 15 (10), 2124–2132.

[14] Lei, J., Liu, S., Guo, H.H., Li, Z.H., Li, J.T., Han, Z.X. (2011). An image reconstruction algorithm based on the semiparametric model for electrical capacitance tomography. *Computers and Mathematics with Applications*, 61 (9), 2843–2853.

[15] Ortiz-Aleman, C., Martin, R., Gamio, J.C. (2004). Reconstruction of permittivity images from capacitance tomography data by using very fast simulated annealing. *Measurement Science and Technology*, 15 (7), 1382–1390.

[16] Warsito, W., Fan, L.S. (2001). Neural network based multi-criterion optimization image reconstruction technique for imaging two-and three-phase flow systems using electrical capacitance tomography. *Measurement Science and Technology*, 12, 2198–2210.

[17] Banasiak, R., Soleimani, M. (2010). Shape based reconstruction of experimental data in 3D electrical capacitance tomography. *NDT & E International*, 43 (3), 241–249.

[18] Cao, Z., Xu, L.J., Fan, W.R., Wang, H.X. (2011). Electrical capacitance tomography for sensors of square cross sections using Calderon's method. *IEEE Transactions on Instrumentation and Measurement*, 60 (3), 900–907.

[19] Li, Y., Yang, W.Q. (2008). Image reconstruction by nonlinear Landweber iteration for complicated distributions. *Measurement Science and Technology*, 19, 1–8.

[20] Cao, Z., Xu, L.J., Wang, H.X. (2010). Electrical capacitance tomography with a non-circular sensor using the dbar method. *Measurement Science and Technology*, 21 (1), 1–6.

[21] Watzenig, D., Brandner, M., Steiner, G. (2007). A particle filter approach for tomographic imaging based on different state-space representations. *Measurement Science and Technology*, 18 (1), 30–40.

[22] Soleimani, M., Vauhkonen, M., Yang, W.Q., Peyton, A., Kim, B.S., Ma, X.D. (2007). Dynamic imaging in electrical capacitance tomography and electromagnetic induction tomography using a Kalman filter. *Measurement Science and Technology*, 18 (11), 3287–3294.

[23] Lei, J., Liu, S., Wang, X.Y. (2012). Dynamic inversion in electrical capacitance tomography using the ensemble Kalman filter. *IET Science, Measurement and Technology*, 6 (1), 63–77.

[24] Soleimani, M., Mitchell, C.N., Banasiak, R., Wajman, R., Adler, A. (2009). Four-dimensional electrical capacitance tomography imaging using experimental data. *Progress in Electromagnetics Research-PIER*, 90 (1), 171–186.

[25] Liu, X. (2011). *Meshfree Method*. Beijing: Science Press.

[26] Liu, G.R. (2010). *Meshfree Methods: Moving Beyond the Finite Element Method* (2nd ed.). Taylor & Francis Group.

[27] Goswami, J.C., Chan, A.K. (1999). *Fundamentals of Wavelet: Theory, Algorithm and Applications*. New York: John Willy & Sons.

[28] Liu, T., Zeng, X.L., Zeng, J. (2006). *An Induction for Practical Wavelet Analysis*. Beijing: National Defense Industry Press.

[29] Misiti, M., Misiti, Y., Oppenheim, G., Poggi, J.M. (2007). *Wavelets and Their Applications*. Herms Science.

[30] Golik, W.L. (1998). Wavelet packets for fast solution of electromagnetic integral equations. *IEEE Transactions on Antennas and Propagation*, 46 (5), 618–624.

[31] Xu, C., Zhao, R.Z., Gan, X.B. (2004). *Wavelet Analysis and Applied Algorithms*. Beijing: Science Press.

[32] Zhang, Z., Shi, Y., Ding, W., Yin, B. (2013). MR images reconstruction based on TVWL2–L1 model. *Journal of Visual Communication and Image Representation*, 24 (2), 187–195.

[33] Rudin, L.I., Osher, S., Fatemi E. (1992). Nonlinear total variation based noise removal algorithms. *Physic D*, 60 (1–4), 259–268.

[34] Li, Y., Osher, S. (2009). A new median formula with applications to PDE based denoising. *Communications in Mathematical Sciences*, 7 (3), 741-753.

[35] Papafitsoros, K., Schonlieb, C.B., Sengul, B. (2013). Combined first and second order total variation inpainting using split Bregman. *Image Processing On Line*, 3, 112–136.

[36] Chan, T.F., Wong, C.K. (2000). Convergence of the alternating minimization algorithm for blind deconvolution. *Linear Algebra and its Applications*, 316 (1–3), 259–285.

[37] Xiao, Y., Zeng, T., Yu, J., Ng, M.K. (2011). Restoration of images corrupted by mixed Gaussian-impulse noise via L1–L0 minimization. *Pattern Recognition*, 44 (8), 1708–1720.

[38] Lv, X.G., Song, Y.Z., Wang, S.X., Le, J. (2013). Image restoration with a high-order total variation minimization method. *Applied Mathematical Modelling*, 37 (16–17), 8210–8224.

[39] Blondel, M., Seki, K., Uehara, K. (2013). Block coordinate descent algorithms for large-scale sparse multiclass classification. *Machine Learning*, 93 (1), 31–52.

[40] Qin, Z., Scheinberg, K., Goldfarb, D. (2013). Efficient block-coordinate descent algorithms for the group lasso. *Mathematical Programming Computation*, 5 (1), 143–169.

[41] Tseng, P. (2001). Convergence of a block coordinate descent method for nondifferentiable minimization. *Journal of Optimization Theory and Applications*, 109 (3), 475–494.

[42] Xu, Y., Yin, W. (2013). A block coordinate descent method for regularized multi-convex optimization with applications to nonnegative tensor factorization and completion. *SIAM Journal on Imaging Sciences*, 6 (3), 1758–1789.

[43] Goldstein, T., Osher, S. (2009). The split Bregman method for L1-regularized problems. *SIAM Journal on Imaging Sciences*, 2 (2), 323–343.

Received April 22, 2015.
Accepted December 1, 2015.